Electronic Modulation of Semimetallic Electrode for 2D van der Waals Devices

Taehun Kim, Jungmoon Lim, Junsung Byeon, Yuljae Cho, Woojong Kim, Jinpyo Hong, Su Jin Heo, Jae Eun Jang, Byung-Sung Kim, John Hong,* Sangyeon Pak,* and SeungNam Cha*

The 2D semimetallic electrodes have been employed to show outstanding contact properties with 2D semiconducting transition-metal dichalcogenides (TMDCs) channel, leading to large enhancement of 2D transistor and phototransistor performance. Herein, an innovative concept is established for a unique 2D semimetallic electrode-2D TMDC channel (2D–2D) device configuration where the electronic structures of 2D semimetallic electrodes are systematically modulated to improve the contact properties with 2D monolayer molybdenum disulfide (MoS_2) channel. The 2D semimetallic copper sulfide (CuS) electrodes are doped with iodine atoms by a direct exposure of iodine gas. The contact properties and charge-transport behavior in the 2D–2D field-effect transistors (FETs) are highly improved, which is attributed to the favorable energy band alignment and associated material properties between the iodine-doped CuS (CuS–I) electrodes and 2D channel. The 2D–2D FETs show a high on current, high on/off ratio, and twofold improvement in mobility. Furthermore, 2D–2D phototransistors and flexible/transparent photodetectors are fabricated using the CuS–I/MoS_2, which also performed outstanding photoresponsivity characteristics and mechanical durability under external bending strain conditions. These findings demonstrate a promising pathway that under the 2D–2D configuration, the electronic modulation by the iodine atoms may enable the development of future 2D electronic applications.

1. Introduction

Electronic and optoelectronic devices composed of 2D layered nanostructures hold great promises for future device system, and their compatibility with various form of factors such as flexible, transparent, and wearable platforms enables even wider and extensive application utilization.[1–4] Especially, 2D transition-metal dichalcogenides (TMDCs) have garnered significant attention as the active channel materials due to their exotic optical and electrical characteristics, outstanding charge-transport properties, and strong light–matter interactions, coupled with high flexibility and transparency.[1–4] In addition, field-effect transistors (FETs) with 2D TMDC channels are expected to show high on/off ratio, low-power consumption, high carrier mobility, and reduced short channel effects,[5] which have spurred to investigate their wide range of applications in nanoelectronics and optoelectronics.

T. Kim, J. Lim, J. Byeon, S. Cha
Department of Physics
Sungkyunkwan University (SKKU)
Suwon, Gyeonggi-do 16419, Republic of Korea
E-mail: chasn@skku.edu

Y. Cho
University of Michigan—Shanghai Jiao Tong University Joint Institute
Shanghai Jiao Tong University
Minhang District, Shanghai 200240, P. R. China

W. Kim, J. Hong
Department of Physics and Division of Nanoscale Semiconductor
Engineering
Hanyang University
Seoul 04763, Republic of Korea

S. Jin Heo, J. Eun Jang
Department of Electrical Engineering and Computer Science
Daegu Gyeongbuk Institute of Science & Technology (DGIST)
Daegu 42988, Republic of Korea

B.-S. Kim
Department of Engineering Science
University of Oxford
Oxford OX1 3PJ, UK

J. Hong
School of Materials Science and Engineering
Kookmin University
Seoul 02707, Republic of Korea
E-mail: johnhong@kookmin.ac.kr

S. Pak
School of Electronic and Electrical Engineering
Hongik University
Seoul 04066, Republic of Korea
E-mail: spak@hongik.ac.kr

Despite such importance for 2D TMDC devices, the electronic performance with TMDC channels was often limited by a large contact resistance at metal–TMDC interface. The main cause of the contact resistance is the induced contact energy barrier, known as Schottky barrier, between metal electrodes and TMDC channels. Especially, this barrier can be attributed to 1) the difference in work function between metal electrodes and the electron affinity of TMDC channels and/or 2) Fermi-level pinning due to unwanted metal–semiconductor interaction or defects at the interface.[6–8] Such unfavorable contact barrier can limit the efficient charge-transport behavior within the device and degrade the overall performance.[6,9] Therefore, it is highly important to reduce the contact barrier between the metallic electrodes and 2D TMDC channels.[7,8]

Few strategies have been proposed to solve the contact problems including metal deposition under ultrahigh vacuum, dry transfer of metal electrode layers, unconventionally employed metals (e.g., In, Bi), and van der Waals contact via metallic 2D materials (e.g., graphene, 1–T MoS_2, and ultrathin transition-metal sulfides).[8–11] Among many strategies, introducing the semimetallic 2D electrodes as a current collector can suppress metal-induced gap states owing to its negligible density of states at the Fermi level, leading to the close match of electron wave function and Fermi levels at the 2D–2D interface. In this regard, the utilization of the semimetallic 2D electrodes can reduce the severe Fermi-level pinning and provide the favorable contact properties compared to the conventional electrode metals (e.g., Ti, Au).[12–14] Moreover, due to its negligible density of states, the electronic structure of semimetallic 2D materials, unlike the metal electrodes, can be easily managed by applying material and chemical modifications (such as doping). The development of the appropriate chemical modification level on the semimetallic 2D electrodes can further minimize the contact barrier problems and optimize the charge-transport parameters with 2D TMDC channels.[15] However, there are no detailed studies describing a simple method to control the electronic properties of semimetallic 2D electrodes in unique 2D–2D device configuration.

We have very recently reported that the semimetallic copper sulfide (CuS) electrodes are effective in forming the low-resistance contact properties with the MoS_2 channels.[1,16,17] In this study, we present a simple and innovative approach to form the optimized contact properties of CuS with the MoS_2 monolayer channel by aligning the energy band and the reinforcing electrode properties of CuS by the chemical modification. Unlike the other metal electrodes, the electronic properties of CuS electrode can be modulated by halide doping due to its semimetallic characteristic. This is achieved through chemically modifying CuS source–drain electrodes via room-temperature iodine doping, which is facile, viable, and nontoxic doping method can be expanded to various device applications. We demonstrate that the contact resistance and the work function were arranged to form the ohmic contact between the 2D MoS_2 channels and iodine-doped CuS (CuS–I) electrodes. The 2D–2D FETs using the CuS–I electrodes and 2D MoS_2 channels showed a high on current ($\mu A \, \mu m^{-1}$), high on/off ratio ($\approx 10^8$), about two-fold improvement in mobility ($11.2 \rightarrow 23 \, cm^2 \, Vs^{-1}$), which is attributed to the improved contact properties by the lowered contact barriers and decreased resistances. We further fabricated phototransistors and flexible/transparent photodetectors using the CuS–I/MoS_2 electrodes which also showed high photo-responsivity characteristics and mechanical durability under external bending strains. These results demonstrated that the iodine chemical modification in the semimetallic 2D electrode can provide an important path toward tailoring the contact properties of various 2D materials using nonmetal electrode materials.

2. Result and Discussion

The iodine doping of CuS is illustrated in the schematics of **Figure 1**a. Note that the iodine molecules of gas phase are bound to the CuS layers to improve their electrical properties and expected that the iodine doping is induced in the CuS electrode. This iodine doping can occur because of the higher electronegativity of iodine compared to that of Cu,[18] similar doping mechanism with previously reported metal-ion-doped CuS.[19–26] The CuS electrode, which is covellite and nanosheet structure, was synthesized based on a room-temperature sulfur activation method which is reported at our previous article.[27] The thickness of CuS was controlled to be $20 \approx 40 \, nm$ which is optimized conditions with a low sheet resistance (Figure 1b). The iodine doping was performed by exposing the CuS electrode to highly active iodine gas which was generated by bulk iodine at room temperature and ambient conditions.

In addition, using the X-ray photoelectron spectroscopy (XPS), it is clearly confirmed that the iodine atoms are chemically reacted and bonded along with the lattice of the CuS nanosheet (Figure 1c–e). Figure 1c,d represents the Cu 2p and S 2p XPS spectra of CuS–I, respectively. The binding energy of Cu^{2+} peaks are deconvoluted to be at 932.02 and 951.80 eV, which correspond to Cu $2p_{3/2}$ and Cu $2p_{1/2}$ states, respectively.[28] Compared to the XPS spectra of CuS, the binding energy of Cu^{2+} peaks are slightly blueshifted, indicating the Cu oxidation stated due to the interaction between Cu and iodine atoms (Figure S1, Supporting Information). The S 2p peaks can also be deconvoluted into two main peaks, which correspond to S^{2-} and S_2^{2-}, and the peak positions are located at 160.8, 161.9, 162.26, and 163.46 eV, respectively.[29] These binding energies depict the typical S oxidation states of CuS, implying that the original oxidation states of S is well maintained after the direct iodine exposure.[27] Figure 1e shows that the iodine-doped CuS nanosheets present the I 3d peak (I $3d_{5/2} = 618.3 \, eV$, I $3d_{3/2} = 629.8 \, eV$). This result shows that the binding energy of the bound iodine is blueshifted compared to the pure iodine molecules as observed at a binding energy of 619.9 and 630.8 eV.[30] These peak shifts demonstrate that the I 3d orbital is varied due to the direct bond with the Cu atoms on CuS. To further support the existence of CuS–I, the energy-dispersive X-ray spectrometer (EDS) mapping was performed for CuS–I (Figure S2, Supporting Information). The mapping images clearly exhibit the presence of the iodine atoms along with the CuS nanosheets. The absorbed iodine elements are also identified by the X-ray diffraction (XRD). Figure 1f shows the XRD patterns of the pristine CuS nanosheet and iodine-doped CuS. From the XRD results, the pristine CuS and CuS–I have both the peaks at 29° and 48°, which strongly corresponds to
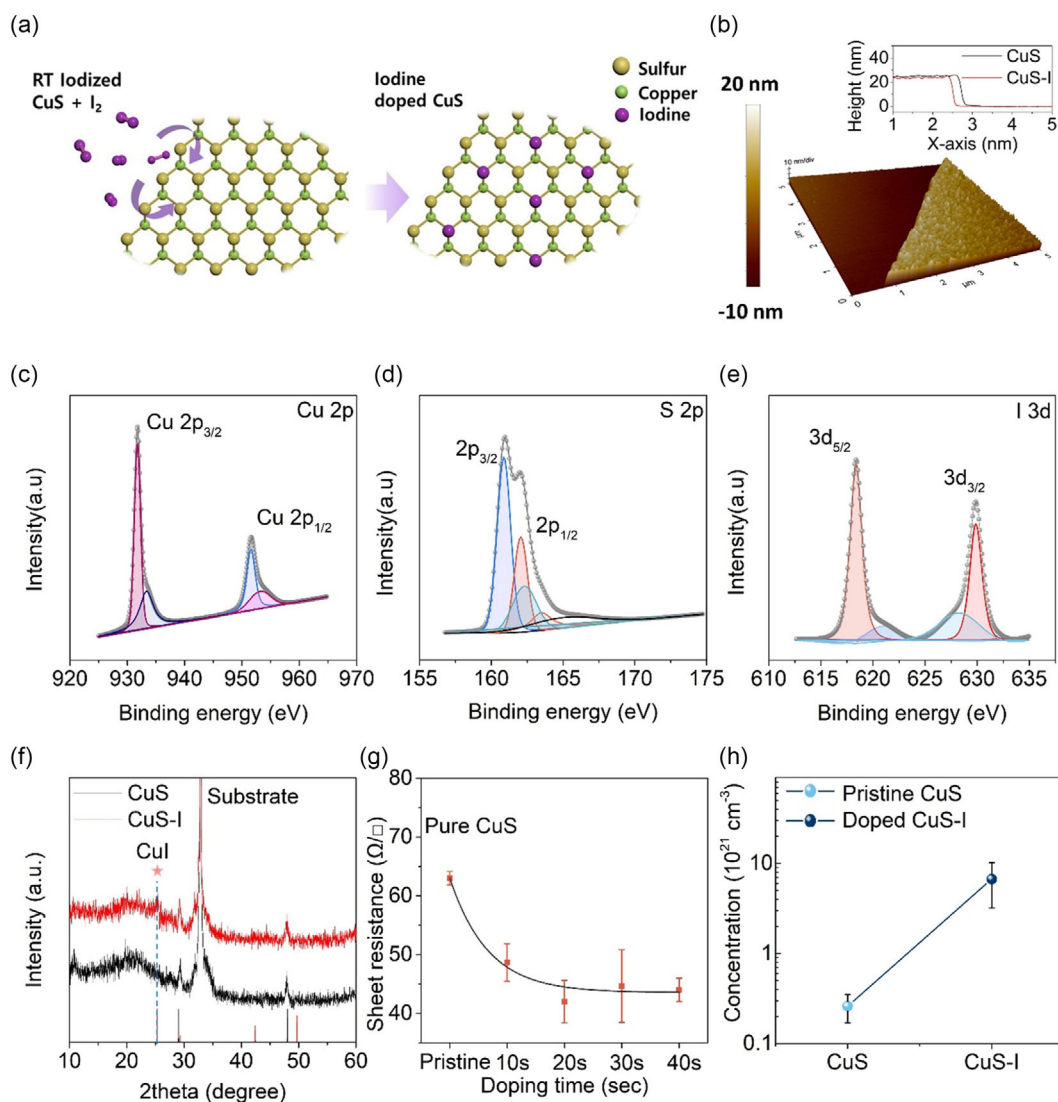
Figure 1. a) Schematic illustration of room-temperature iodine-doping synthesis. b) A 3D Atomic force microscopy (AFM) topography image of the CuS–I nanosheet with 20 nm (inset shows the thickness profile of pristine CuS and CuS–I nanosheet). c–e) X-ray photoelectron spectrum (XPS) of c) Cu 2p, d) S 2p, and e) I 3 d of iodine-doped CuS. The XPS results confirm that iodine ions are bound to CuS. f) X-ray diffraction (XRD) spectrum of CuS and iodine-doped CuS. The CuI peak around 25.3° is observed after iodized CuS nanosheet. g) The sheet resistance of CuS–I nanosheet with various doping time. h) The concentration of the pristine CuS and iodine-doped CuS nanosheet.

CuS (1 0 2) and (1 1 0) lattice (JCPDS No. 06-0464), respectively. It can be observed that small portion of CuI peak was also appeared at 25.5° which correspond to CuI (1 1 1) lattice (JCPDS No.06-0246) after exposing the iodine gas.[31]

To confirm the influence of the iodine doping on the electrical properties of the CuS electrodes, we measured the sheet resistance of the CuS and CuS–I electrodes using a 4-probe measurement as shown in Figure 1g. It is found that the sheet resistance is gradually decreased from 63 to 42 $\Omega \square^{-1}$, which is about 33% improvement in the sheet resistance, upon the iodine doping and saturation. The doping time–dependent iodine atomic concentration was also saturated after 30 s (Figure S3, Supporting Information). We also compared the carrier concentration of the pristine CuS and CuS–I electrodes by a Hall effect

measurement (Figure 1h). The hole concentration was found to be 0.26×10^{21} and 6.7×10^{21} cm^{-3} for the CuS and iodine-doped CuS electrodes, respectively. These enhanced properties can be attributed to the induced iodine molecules that are adsorbed to the sulfur vacancy sites in CuS, resulting in the increase of the hole concentration.[21, 32] Such changes in the electrical properties of the CuS nanosheet upon the iodine doping indicate that the iodine is an effective in modulating the charge carrier densities of CuS electrode and leads to more metallic electrical properties (Figure S4, Supporting Information).

To identify the energy level of the CuS and CuS–I electrodes and the corresponding band alignment, we investigated the work function of the CuS and CuS–I electrodes using ultraviolet
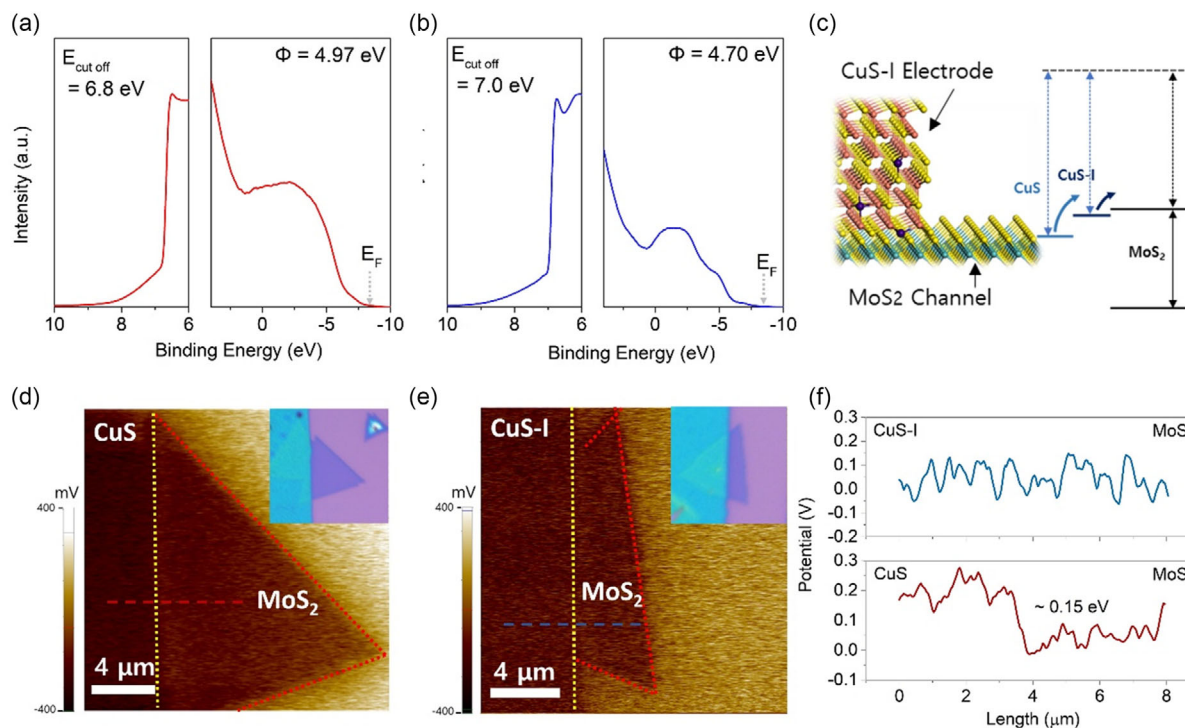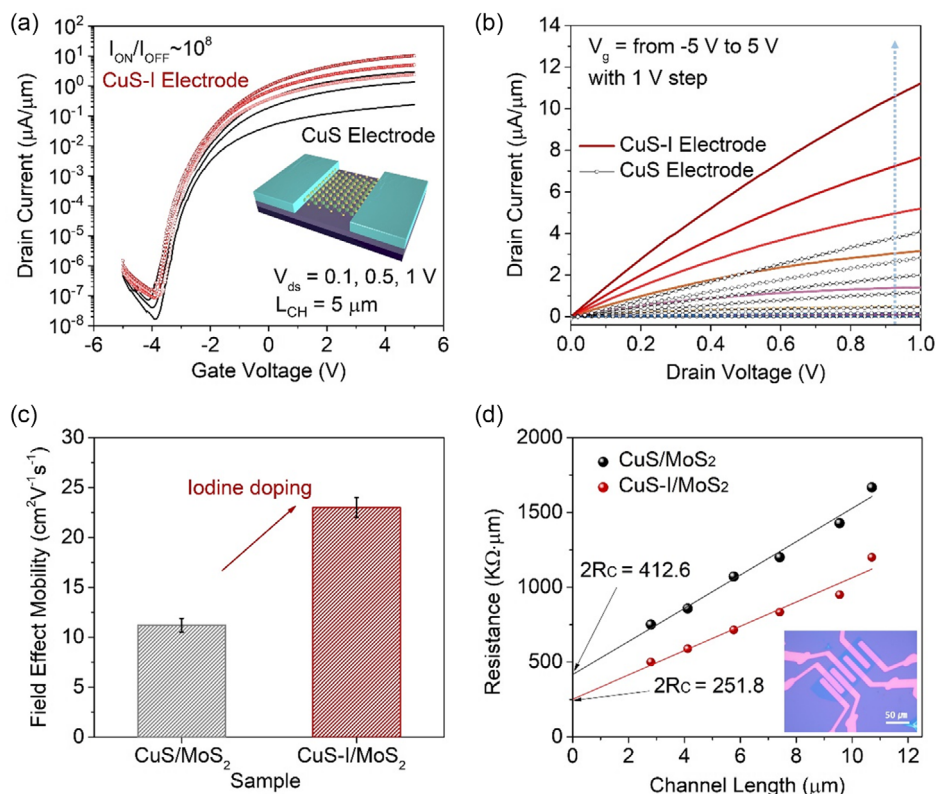
Figure 2. a) The pure CuS nanosheet work function and b) iodine-doped CuS nanosheet work function which were measured by ultraviolet photoelectron spectroscopy (UPS). The work function of treated CuS (4.8 eV) is similar or slightly lower than MoS$_2$ (5.2 eV). c) MoS$_2$, CuS, and CuS–I work function. It is shown that MoS$_2$/electrode band diagram in the inset. d,e) Kelvin probe force microscopy (KPFM) image of d) CuS/MoS$_2$ and e) CuS–I/MoS$_2$ devices. It shows interface work function differences between electrode and channel. f) KPFM line scan, denoted by a red dotted line in (d) and (e), which show work function difference of electrode–channel.

photoelectron spectroscopy (UPS) as shown in **Figure 2**a,b. The work function of the pristine CuS and CuS–I electrodes was measured to be 4.97 and 4.70 eV, respectively. As shown in the schematics of Figure 2c, after the iodine doping, the work function of the CuS–I electrodes decreases, resulting in the lowering of the Schottky barrier and forming ohmic contact between the CuS–I electrodes and the 2D MoS$_2$ channels.[33,34] To confirm the band alignment and further understand the effects of the chemical modification, we measured and compared the 2D work function mapping images of the CuS/MoS$_2$ and CuS–I/MoS$_2$ heterojunctions using a kelvin probe force microscope (KPFM) as shown in Figure 2d,e. The 2D work function mapping were performed from the heterojunctions shown in the inset images of Figure 2d,e. The KPFM image in Figure 2d shows the clear distinction of potential difference between CuS electrodes and MoS$_2$ monolayer channel, as observed by the direct color difference. The noticeable potential offset of around 0.15 eV and the corresponding depletion region were confirmed as shown in the extracted line profile shown in Figure 2f. On the contrary, the KPFM image in Figure 2e shows that the potential difference between the CuS–I electrodes and MoS$_2$ monolayer was decreased, as observed by the negligible color difference and reduced potential offset shown in Figure 2f. These results clearly demonstrate the well-aligned band energies for CuS–I/MoS$_2$ compared to CuS/MoS$_2$.

To understand in detail how the reduced contact barrier affects the electrical properties of MoS$_2$ FETs, we have fabricated and

compared the transistor performance of CuS/MoS$_2$ and CuS–I/MoS$_2$ FETs. The FETs were fabricated on HfO$_2$/Si substrate as shown in the inset schematic picture of **Figure 3**a. Figure 3a presents the representative drain current versus gate voltage of CuS/MoS$_2$ and CuS–I/MoS$_2$ FETs, which is shown in a logarithmic scale at drain voltages of 0.1, 0.5, and 1 V. Both CuS/MoS$_2$ and CuS–I/MoS$_2$ FETs exhibit n-type characteristics, steep subthreshold swing, low off currents, high on currents, and large on/off ratio, indicating that both electrodes are effective in forming low electron barrier with the MoS$_2$ channel. Interestingly, the CuS–I/MoS$_2$ FET showed orders of magnitude higher on current than the CuS/MoS$_2$ FET, reaching up to 10.3 µA µm^{-1}. From the output curve in Figure 3b, it can be also clearly seen that the on current was largely increased for the CuS–I/MoS$_2$ FET compared to that of CuS/MoS$_2$ FET, indicating enhanced charge-transport characteristics with reduced contact barriers. In addition, we compared electrical properties of CuS–I/MoS2 FET based on MoS2 channel (Table S1, Supporting Information).

From the transfer characteristics in Figure 3a, we have estimated a field-effect mobility using $\mu_{FE} = \frac{L}{W C_{ox} V_{ds}} \frac{dI_{ds}}{dV_{gs}}$, where L and W are channel length and width, respectively, and C_{ox} is the gate capacitance of 309.9 nF cm^{-2}, which are compared in Figure 3c. The room temperature, back-gated field-effect mobility was measured to be 11.2 cm^2 Vs^{-1} for the CuS/MoS$_2$ FET and 23 cm^2 Vs^{-1} for the CuS–I/MoS$_2$ FET, which is about

ADVANCED
SCIENCE NEWS
www.advancedsciencenews.com

small
structures
www.small-structures.com

Figure 3. a) Transfer curves at 0.1, 0.5, 1 V source–drain bias in logarithmic scale. On current of CuS–I/MoS$_2$ field-effect transistor (FET) is higher than the CuS/MoS$_2$ FET ($\approx$10.3 µA µm^{-1}) b) Output curves at various gate voltages (-5–$+5$ V) of the CuS–I/MoS$_2$ electrode device. c) The field-effect mobility of CuS/MoS$_2$ and CuS–I/MoS$_2$ electrodes. After the doping process, the field-effect mobility of the CuS–I device is higher than the pure CuS electrode device. d) The contact resistance of CuS/MoS$_2$ and CuS–I/MoS$_2$. The y-intercept of the linear fit (Rc) is the contact resistance and inset shows the device of transfer-length measurement (TLM) measurement.

twofold increase in the mobility. The improvement of mobility as well as the on current for CuS–I/MoS$_2$ can be attributed to the enhanced contact properties resulting from alignment of energy levels as also provided using UPS and KPFM measurements in Figure 2. To further gain insight into the enhanced contact properties in CuS–I/MoS$_2$ FET, we have measured and compared the contact resistance (R_C) of the CuS/MoS$_2$ and CuS–I/MoS$_2$ FETs using transfer-length measurement (TLM) as shown in Figure 3d. The TLM measurements show a good linear fit when the total device resistance, normalized by the channel width, was plotted in terms of channel length, demonstrating the uniform contact properties. The γ-intercept of the linear fit is the total contact resistance ($2R_C$), and the R_C was found to be 206.3 kΩ µm for CuS/MoS$_2$ FET and 125.9 kΩ µm for CuS–I/MoS$_2$ FET. Such decrease in the R_C for the CuS–I/MoS$_2$ FET can be attributed to the decreased contact barrier height induced by lowering of work function of CuS–I electrode and decreased resistance of CuS–I electrode.[33,34]

To further confirm the effect of the contact engineering, we now consider the phototransistor performance of the CuS–I/MoS$_2$ phototransistor. It should be noted that the phototransistor with reduced contact barriers can lead to high photoresponsivity due to the enhanced photo-generated carrier transport/transfer from MoS$_2$ to the electrode.[6,35] **Figure 4**a,b, Supporting Information, shows the schematic of the phototransistor device

configuration and the transfer curve of the CuS–I/MoS$_2$ phototransistor under various illumination intensities, respectively. The incident laser power is estimated considering the laser spot size with a diameter of 2 mm. Based on the Figure 4b, we can calculate the photoresponsivity using the equation $R = \frac{I_{ph}}{P}$, where I_{ph} is the photocurrent and P is the incident laser power on the effective device area.[1,36] The photoresponsivity of the CuS–I/ MoS$_2$ phototransistor was plotted with respective to the incident laser power at $V_g = -1, 0, 1$ V, which was compared with the photoresponsivity of the CuS/MoS$_2$ phototransistor as shown in Figure 4c. It can be clearly shown that the photoresponsivity shows linear relationship with the incident power and is higher for the CuS–I/MoS$_2$ phototransistor compared to the CuS/MoS$_2$ phototransistor at all gate biases. Furthermore, we found that the photoresponsivity as high as $R = 2.25 \times 10^4$ A W^{-1} was calculated at $V_g = +5$ V and $P = 3.4 \times 10^{-3}$ mW cm^{-2} as shown in Figure 4d (Figure S5, Supporting Information). The specific detectivity, $D^* = \frac{\sqrt{AB}}{NEP}$, with respective to the gate voltages was also measured considering the device active area (A), noise bandwidth (B), and NEP (NEP $= \frac{i_n}{R}$, assuming the shot noise is the major noise current). We found maximum detectivity up to $D^* = 1.16 \times 10^{11}$ jones under negative polarity back-gate voltages, which can be attributed to the high photoresponsivity as well as low dark current. Furthermore, the photoresponsivity
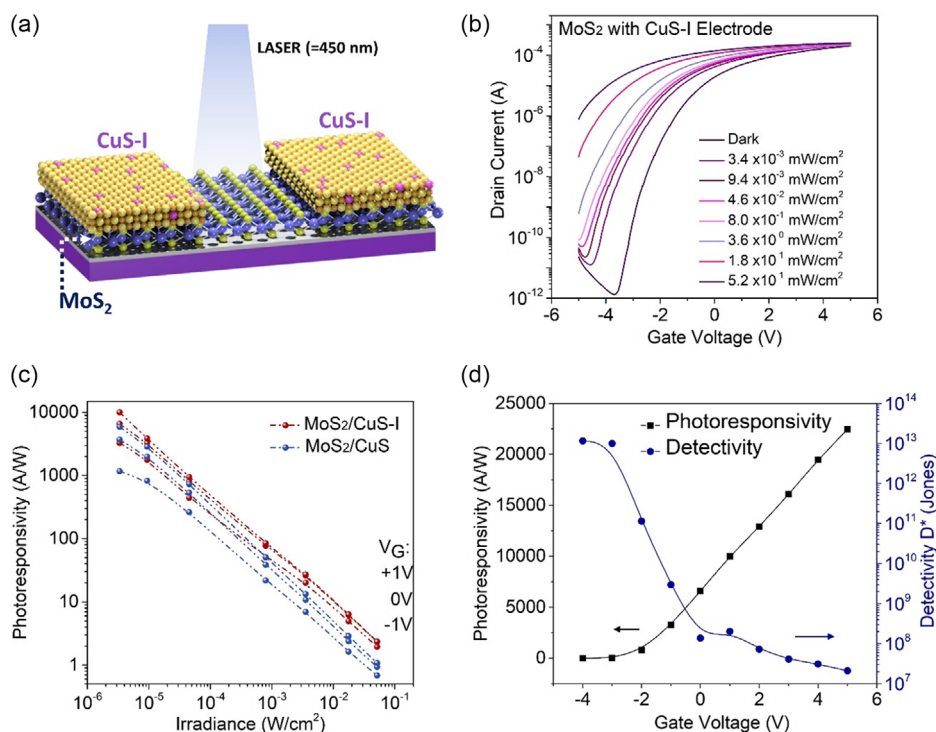
Figure 4. a) The schematic of CuS–I/MoS$_2$ phototransistor with the laser ($\lambda = 450$ nm) illumination. b) The drain current of CuS–I/MoS$_2$ phototransistor with different gate voltage ($-5 \approx 5$ V) under different laser power densities (dark to 52 mW cm^{-2}). c) The photoresponsivity with various incident laser power at different gate voltage (-1, 0, 1 V). d) Photoresponsivity (left axis) and detectivity (right axis) of CuS–I/MoS$_2$ device as a function of gate voltages.

and detectivity of our phototransistor are significantly better than the other devices with MoS$_2$ channel (Table S2, Supporting Information, for comparison)

The attractive features of 2D materials for electrodes and channels in terms of their outstanding electrical, optical, and mechanical properties enable us to develop highly flexible and transparent optoelectronic devices based on those 2D materials. The transmittance of CuS–I nanosheet (<20 nm) versus pristine CuS is shown in Figure S6, Supporting Information. The CuS–I nanosheet has outstanding transmittance above 90% in the visible range, while maintaining ultrathin thickness of 20 nm. The ultrathin CuS–I electrode not only possess outstanding electrical properties but also outstanding stability under mechanical strain, making them highly suitable for flexible device applications. As shown in **Figure 5**a, the sheet resistance of CuS–I electrode was measured under different bending strain. It was found that the sheet resistance of the CuS–I electrode was well maintained up to 10^5 bending cycles at 3 mm bending radius as shown in the inset image of Figure 5a.

Using the flexible, ultrathin CuS–I electrode, we fabricated CuS–I/MoS$_2$ flexible photodetectors on PET substrate as shown in Figure 5b. The inset image of Figure 5b is the optical microscope image of the CuS–I/MoS$_2$. The time domain photocurrent of CuS–I/MoS$_2$ flexible photodetector was measured under 450 nm laser illumination which was turned on and off repeatedly for 5 s as shown in Figure 5c, showing stable and repeatable photocurrent. The mechanical stability of the CuS–I/MoS$_2$ photodetector was measured as shown in Figure 5d.

The photocurrent and dark current of the device were well maintained with only a little variation in the magnitude when the device is bent up to 10^4 bending cycles. Furthermore, we measured the electrical stability under the ambient condition with four-probe measurement and KPFM (Figure S7, Supporting Information). Such high stability under mechanical strain and electrical stability can be attributed to the ultrathin nature of the CuS–I electrode and the MoS$_2$ monolayer, which is highly suitable for future flexible and transparent optoelectronic device applications.

3. Conclusion

In summary, we have demonstrated that a semimetallic and iodine-doped copper sulfide electrode has been successfully prepared via an ultrafast and room-temperature gas-exposure process. The addition of iodine atoms can effectively reduce the contact barrier at the interface with 2D MoS$_2$ channel and, subsequently, greatly improve the electrical properties of transistors. This is because the electrical properties and the energy levels of the CuS electrode is favorably modified, and the intrinsic Schottky barrier height on the interface of CuS–I/MoS$_2$ is decreased, and the charge-transfer mechanism is improved. Moreover, the photoelectrical properties of the CuS–I/MoS$_2$ device were further examined, and the enhanced photodetector performance was analyzed compared to that of CuS/MoS$_2$ device. Thus, we expect that this study on semimetallic 2D
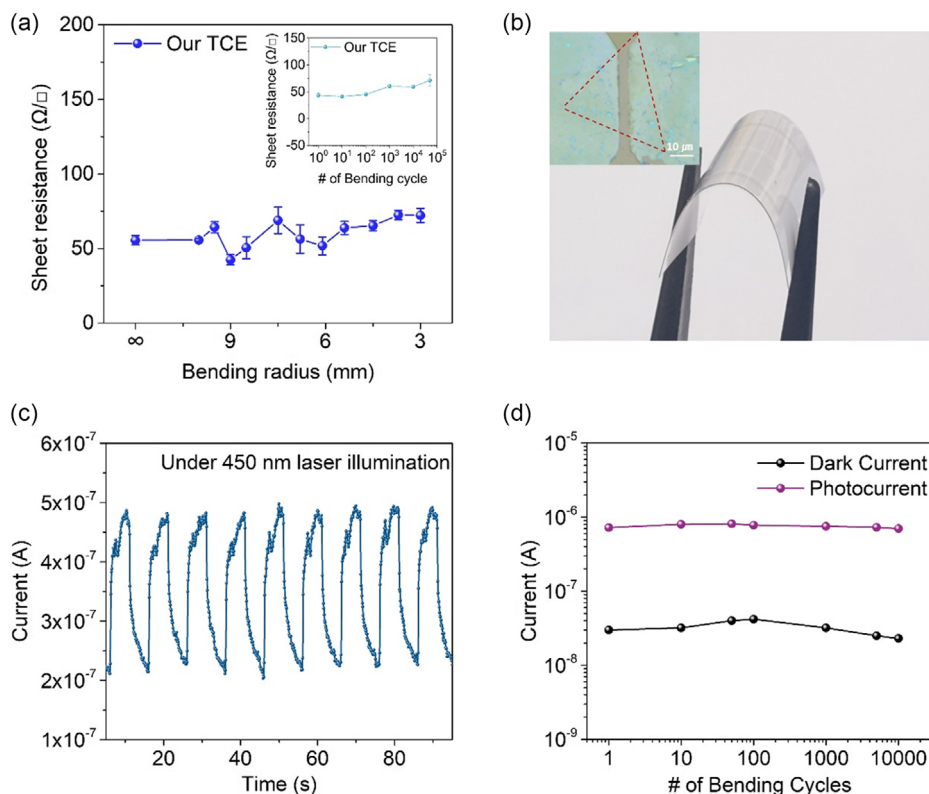
Figure 5. a) The sheet resistance of CuS–I nanosheet with various bending radius. In addition, it is found that it has outstanding bending properties up to 10^5 bending cycles at 3 mm bending radius as shown in inset. b) CuS–I/MoS$_2$ photodetectors on PET substrate and the optical image of the photodetector (inset). c) The time domain photocurrent of CuS–I/MoS$_2$ flexible photodetector was measured under 450 nm laser illumination which was turned on and off frequently for 5 s. d) The photocurrent and dark current of the device were tested under mechanical strain. It is shown that it has only a little variation when the device is bent up to 10^4 bending cycles at 3 mm bending radius.

electrode structure and its doping conditions will be extensively utilized, providing highly flexible and efficient electronic device applications.

Conflict of Interest

The authors declare no conflict of interest.

Data Availability Statement

The data that support the findings of this study are available from the corresponding author upon reasonable request.

[1] S. Pak, S. Jang, T. Kim, J. Lim, J. S. Hwang, Y. Cho, H. Chang, A. R. Jang, K. H. Park, J. Hong, *Adv. Mater.* **2021**, *33*, 2102091.

[2] J. Lee, S. Pak, Y.-W. Lee, Y. Cho, J. Hong, P. Giraud, H. S. Shin, S. M. Morris, J. I. Sohn, S. Cha, *Nat. Commun.* **2017**, *8*, 1.

[3] S. Pak, J. Lee, Y.-W. Lee, A.-R. Jang, S. Ahn, K. Y. Ma, Y. Cho, J. Hong, S. Lee, H. Y. Jeong, *Nano Lett.* **2017**, *17*, 5634.

[4] S. Pak, A.-R. Jang, J. Lee, J. Hong, P. Giraud, S. Lee, Y. Cho, G.-H. An, Y.-W. Lee, H. S. Shin, *Nanoscale* **2019**, *11*, 4726.

[5] J. Wang, Q. Yao, C. W. Huang, X. Zou, L. Liao, S. Chen, Z. Fan, K. Zhang, W. Wu, X. Xiao, *Adv. Mater.* **2016**, *28*, 8302.

[6] A. Allain, J. Kang, K. Banerjee, A. Kis, *Nat. Mater.* **2015**, *14*, 1195.

[7] H.-J. Chuang, B. Chamlagain, M. Koehler, M. M. Perera, J. Yan, D. Mandrus, D. Tomanek, Z. Zhou, *Nano Lett.* **2016**, *16*, 1896.

[8] Y. Liu, J. Guo, E. Zhu, L. Liao, S.-J. Lee, M. Ding, I. Shakir, V. Gambin, Y. Huang, X. Duan, *Nature* **2018**, *557*, 696.

[9] Y. Zhao, K. Xu, F. Pan, C. Zhou, F. Zhou, Y. Chai, *Adv. Funct. Mater.* **2017**, *27*, 1603484.

[10] Y. Wang, J. C. Kim, R. J. Wu, J. Martinez, X. Song, J. Yang, F. Zhao, A. Mkhoyan, H. Y. Jeong, M. Chhowalla, *Nature* **2019**, *568*, 70.

[11] Y. Liu, X. Duan, Y. Huang, X. Duan, *Chem. Soc. Rev.* **2018**, *47*, 6388.

[12] B. Radisavljevic, M. B. Whitwick, A. Kis, *ACS Nano* **2011**, *5*, 9934.

[13] H. S. Lee, S.-W. Min, Y.-G. Chang, M. K. Park, T. Nam, H. Kim, J. H. Kim, S. Ryu, S. Im, *Nano Lett.* **2012**, *12*, 3695.

[14] B. Radisavljevic, A. Kis, *Nat. Mater.* **2013**, *12*, 815.

[15] Y. Liu, H. Wu, H.-C. Cheng, S. Yang, E. Zhu, Q. He, M. Ding, D. Li, J. Guo, N. O. Weiss, *Nano Lett.* **2015**, *15*, 3030.

[16] A. Morales-García, A. L. Soares Jr., E. C. Dos Santos, H. A. de Abreu, H. l. A. Duarte, *J. Phys. Chem. A* **2014**, *118*, 5823.

[17] T. Kim, S. Pak, J. Lim, J. S. Hwang, K.-H. Park, B.-S. Kim, S. Cha, *ACS Appl. Mater. Interfaces* **2022**, *14*, 13499.

[18] P. Luo, F. Zhuge, Q. Zhang, Y. Chen, L. Lv, Y. Huang, H. Li, T. Zhai, *Nanoscale Horiz* **2019**, *4*, 26.

[19] L. Yang, K. Majumdar, H. Liu, Y. Du, H. Wu, M. Hatzistergos, P. Hung, R. Tieckelmann, W. Tsai, C. Hobbs, *Nano Lett.* **2014**, *14*, 6275.

[20] M. Inoue, C. Cruz-Vazquez, M. Inoue, K. Nebesny, Q. Fernando, *Synth. Met.* **1993**, *57*, 3748.

[21] J. Jing, X. Gu, S. Zhang, J. Sun, Y. Chen, T. Sun, *Cryst. Eng. Comm* **2019**, *21*, 4969.

[22] P. Wang, Y. Gao, P. Li, X. Zhang, H. Niu, Z. Zheng, *ACS Appl. Mater. Interfaces* **2016**, *8*, 15820.

[23] R. Zeinodin, F. Jamali-Sheini, *Physica B* **2019**, *570*, 148.

[24] S. Pak, J. Son, T. Kim, J. Lim, J. Hong, Y. Lim, C.-J. Heo, K.-B. Park, Y. W. Jin, K.-H. Park, *Nanotechnology* **2022**, *34*, 015702.

[25] S. Pak, *Nanomaterials* **2022**, *12*, 2893.

[26] J. Lim, T. Kim, J. Byeon, K.-H. Park, J. Hong, S. Pak, S. Cha, *J. Mater. Chem. A* **2022**, *10*, 23274.

[27] J. Hong, B.-S. Kim, B. Hou, S. Pak, T. Kim, A.-R. Jang, Y. Cho, S. Lee, G.-H. An, J. E. Jang, *ACS Appl. Mater. Interfaces* **2021**, *13*, 4244.

[28] N. Karikalan, R. Karthik, S. Chen, *Sci. Rep.* **2017**, *7*, 2494.

[29] J. Ludwig, L. An, B. Pattengale, Q. Kong, X. Zhang, P. Xi, J. Huang, *J. Phys. Chem. Lett.* **2015**, *6*, 2671.

[30] J. Li, X. Li, D. Xiong, Y. Hao, H. Kou, W. Liu, D. Li, Z. Niu, *RSC Adv.* **2017**, *7*, 55060.

[31] B. N. Ezealigo, A. C. Nwanya, A. Simo, R. U. Osuji, R. Bucher, M. Maaza, F. I. Ezema, *Arab. J. Chem.* **2019**, *12*, 5380.

[32] Y. Bekenstein, K. Vinokurov, S. Keren-Zur, I. Hadar, U. Schilt, U. Raviv, O. Millo, U. Banin, *Nano Lett.* **2014**, *14*, 1349.

[33] Q. Wang, B. Deng, X. Shi, *Phys. Chem. Chem. Phys.* **2017**, *19*, 26151.

[34] N. Kaushik, D. Karmakar, A. Nipane, S. Karande, S. Lodha, *ACS Appl. Mater. interfaces* **2016**, *8*, 256.

[35] S. Bhattacharjee, K. L. Ganapathi, D. N. Nath, N. Bhat, *IEEE Trans. Electron Devices* **2016**, *63*, 2556.

[36] S. Pak, J. Lee, A. R. Jang, S. Kim, K. H. Park, J. I. Sohn, S. Cha, *Adv. Funct. Mater.* **2020**, *30*, 2002023.

2200274 (8 of 8)